Supporting Information

Tailoring Magnetocaloric Effects in 2D Transition-Metal Phthalocyanines via Halogen Substitution

Peng Wang,[1] Nanshu Liu, [1] Hongkuan Yuan, [1] Xue Jiang,[2,3] and Jijun Zhao[2,3]*

1 Chongqing Key Laboratory of Micro & Nano Structure Optoelectronics, School of Physical Science and Technology, Southwest University, Chongqing 400715, China

2 Guangdong Basic Research Center of Excellence for Structure and Fundamental Interactions of Matter, Guangdong Provincial Key Laboratory of Quantum Engineering and Quantum Materials, School of Physics, South China Normal University, Guangzhou 510006, China

3 Guangdong-Hong Kong Joint Laboratory of Quantum Matter, Frontier Research Institute for Physics, South China Normal University, Guangzhou 510006, China

E-mail: jiangx@scnu.edu.cn

Determination of Magnetic Ground State and Magnetic Coupling Parameters

We compare the energies of the ferromagnetic (FM) and two possible antiferromagnetic (AFM) structures (Néel AFM and Stripy AFM, as shown in Fig. S4) in a 2×2 supercell. The magnetic structure with lowest energy is determined as the magnetic ground state. By considering the coupling between nearest (J_1) and next-nearest (J_2) neighbors, the magnetic coupling parameters are then calculated by mapping the energy to the Heisenberg spin model:

$$H = H_0 - \sum_{<i,j>} J_1 \overrightarrow{S_i} \bullet \overrightarrow{S_j} - \sum_{<k,l>} J_2 \overrightarrow{S_k} \bullet \overrightarrow{S_l} \quad \text{(S1)}$$

Here, $\overrightarrow{S_i}$ is the spin vector at site *i*. H_0 is the nonmagnetic part of Hamiltonian. The energies of the magnetic structures considered can be expressed as:

$$E_{FM} = E_0 - 8J_1S^2 - 8J_2S^2 \quad \text{(S2)}$$

$$E_{Neel} = E_0 + 8J_1S^2 - 8J_2S^2 \quad \text{(S3)}$$

$$E_{Stripy} = E_0 + 8J_2S^2 \quad \text{(S4)}$$

The values of J_1 and J_2 can be calculated from:

$$J_1 = \frac{1}{16S^2}\left(E_{\text{Neel}} - E_{\text{FM}}\right) \quad \text{(S5)}$$

$$J_2 = \frac{1}{32S^2}\left(2E_{\text{Stripy}} - E_{\text{Neel}} - E_{\text{FM}}\right) \quad \text{(S6)}$$

In practice, the total energies of the FM, Néel AFM, and Stripy AFM configurations (E_{FM}, $E_{Néel}$, and E_{Stripy}) are obtained from spin-polarized DFT calculations in a 2×2 supercell with collinear spin arrangements along the out-of-plane direction. The above three equations form a linear system with three unknowns (H_0, J_1, and J_2), from which J_1 and J_2 are uniquely determined.

The anisotropy constant *A* in the spin Hamiltonian is derived from the magnetocrystalline anisotropy energy (MAE). The MAE is calculated as the total energy difference between in-plane and out-of-plane magnetization directions, *i.e.*, MAE = $E_{in\text{-}plane} - E_{out\text{-}of\text{-}plane}$, where spin-orbit coupling (SOC) is included self-consistently. The calculations are performed with a tight energy convergence criterion of 10^{-7} eV to ensure the accuracy of the small energy differences involved. The anisotropy constant *A* per magnetic ion is then obtained by mapping the MAE onto the anisotropy term of the spin Hamiltonian. Specifically, for a system with uniaxial magnetic anisotropy, A = MAE/S^2, where *S* is the spin quantum number of the magnetic ion.

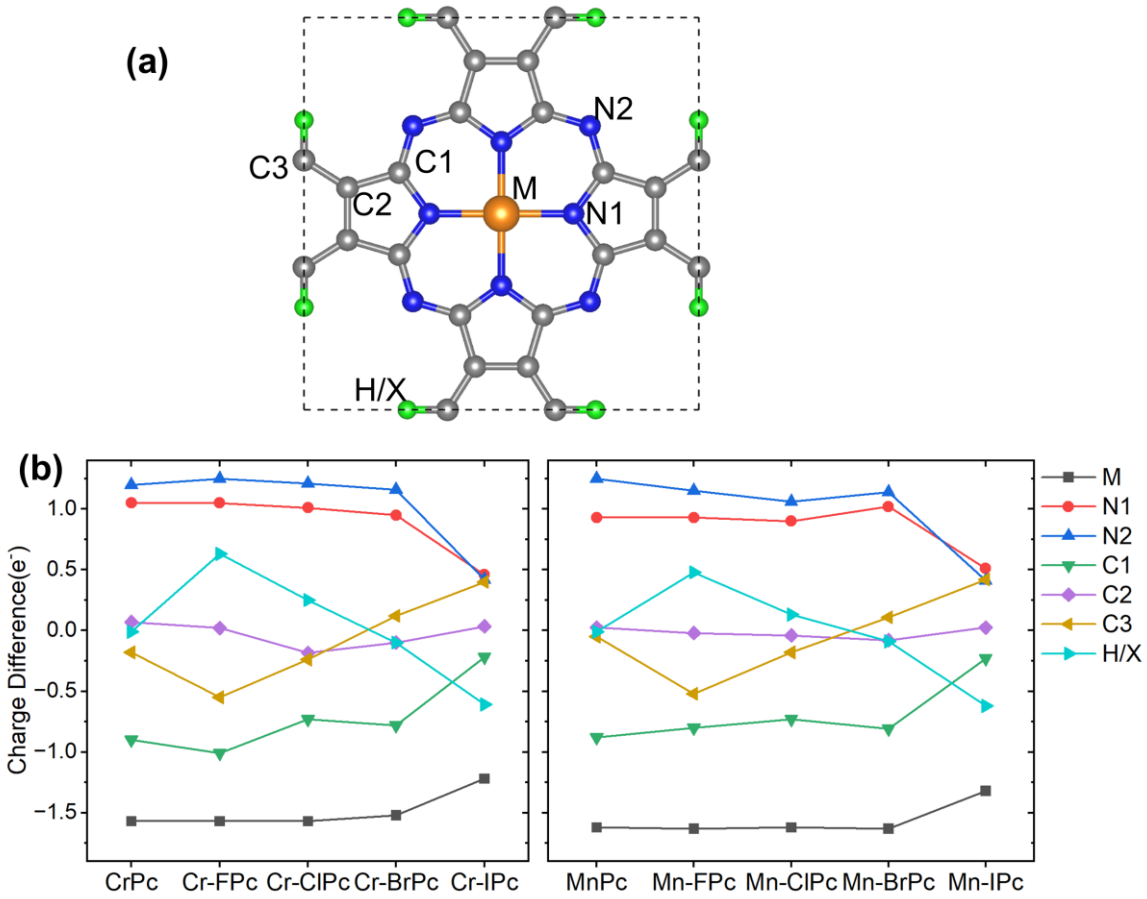

Fig. S1. Atomic-site labeling and halogen-substitution-induced charge redistribution in MPc and M-XPc frameworks. (a) Schematic labeling the atomic sites in the MPc and M-XPc frameworks. Based on their symmetry, two nitrogen sites (N1 and N2) and three carbon sites (C1, C2, and C3) are considered. (b) Evolution of the charge difference with respect to different substituted halogen atoms for Cr-based (left panel) and Mn-based (right panel) frameworks.

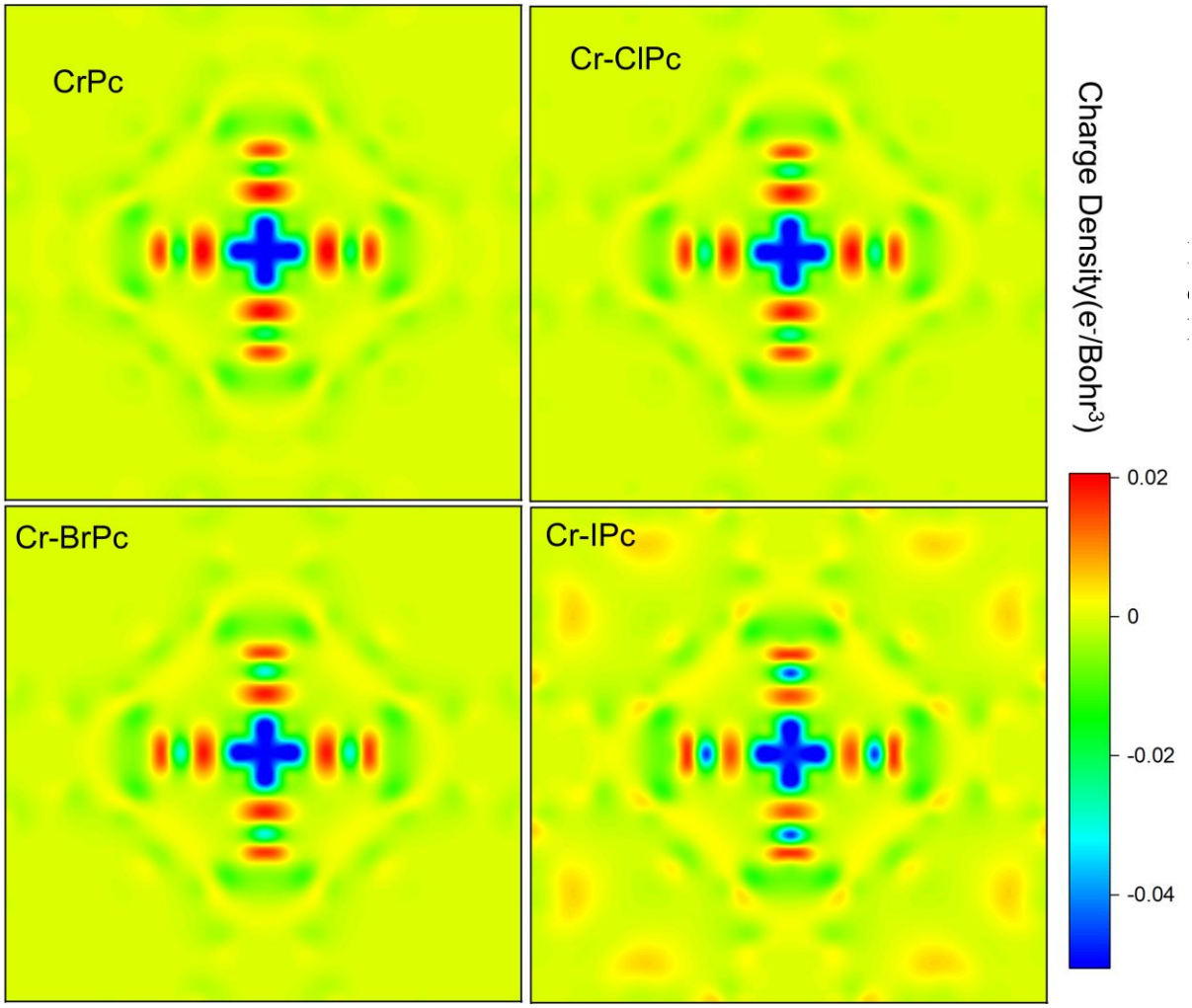

Fig. S2. Halogen-substitution-induced charge-density differences in Cr-based frameworks. The two-dimensional charge-density difference (Δρ) slices are shown for CrPc, Cr-ClPc, Cr-BrPc, and Cr-IPc.

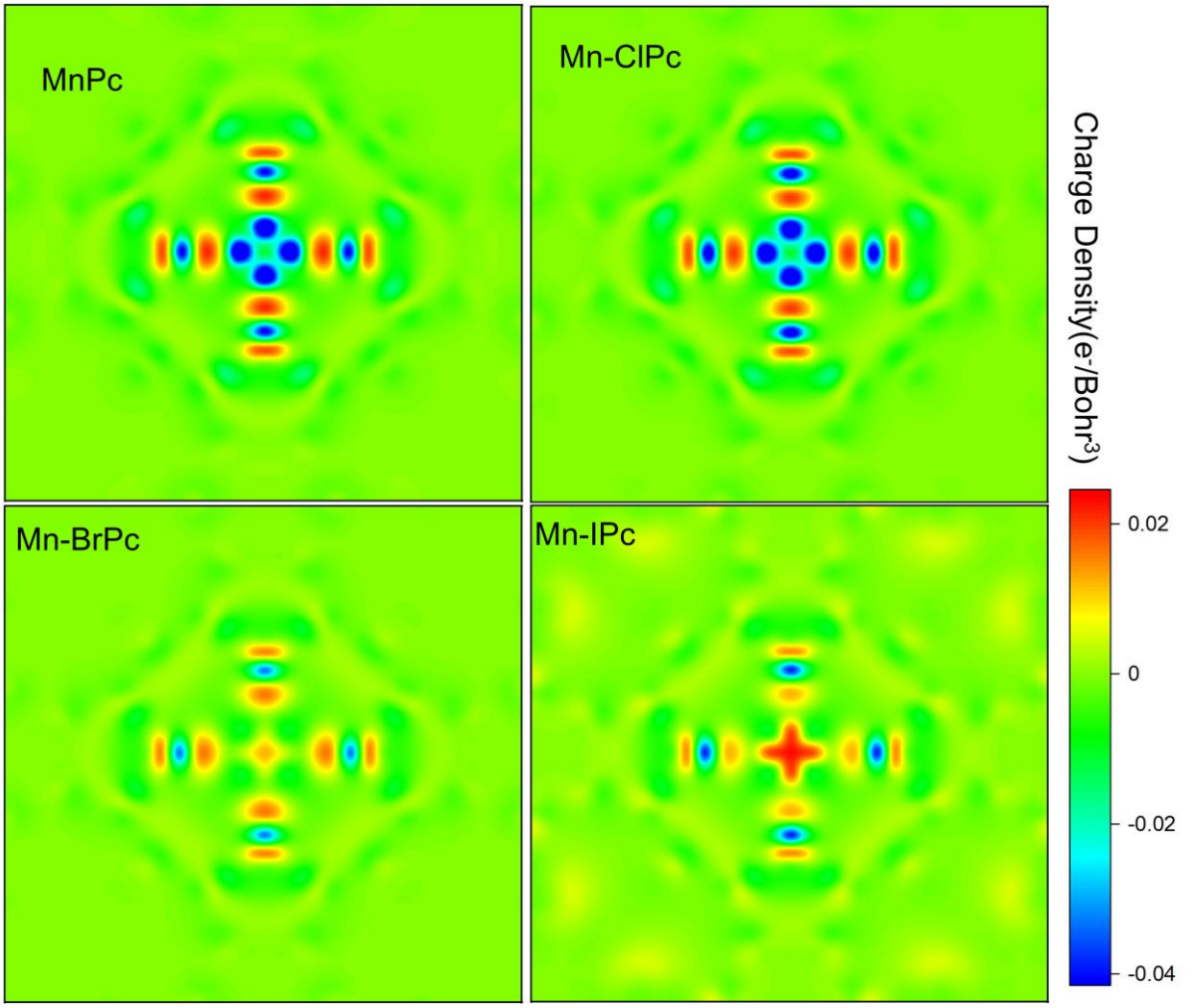

Fig. S3. Halogen-substitution-induced charge-density differences in Mn-based frameworks. The two-dimensional charge-density difference (Δρ) slices are shown for MnPc, Mn-ClPc, Mn-BrPc, and Mn-IPc.

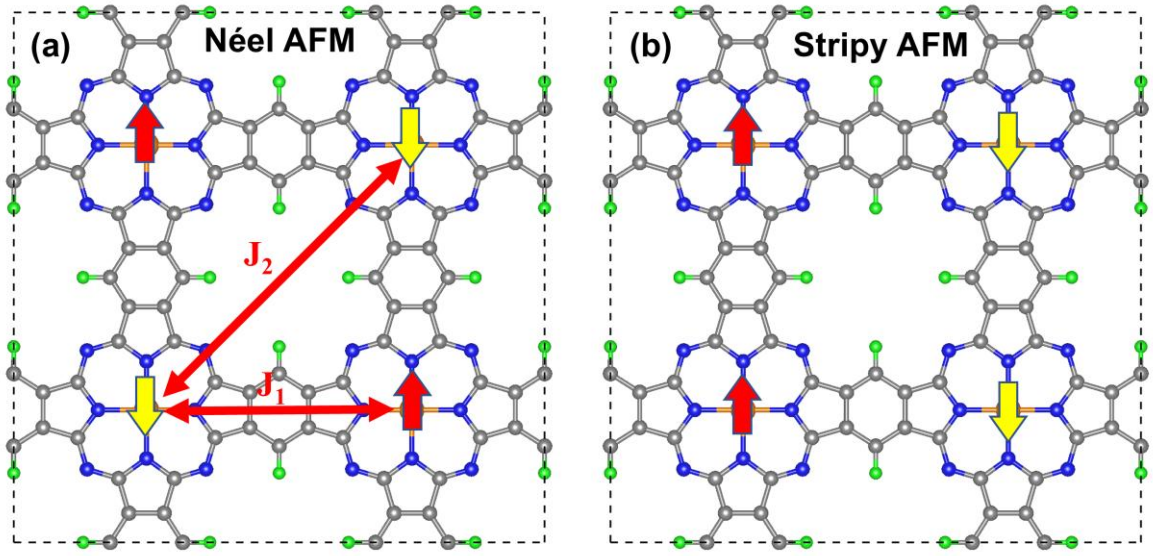

Fig. S4. Antiferromagnetic configurations and exchange interactions in a 2×2 supercell. Panel (a) shows the Néel antiferromagnetic configuration, with double-headed arrows indicating the nearest-neighbor (J_1) and next-nearest-neighbor (J_2) exchange interactions. Panel (b) shows the stripy antiferromagnetic configuration. Upward and downward arrows indicate the orientations of the on-site spins.

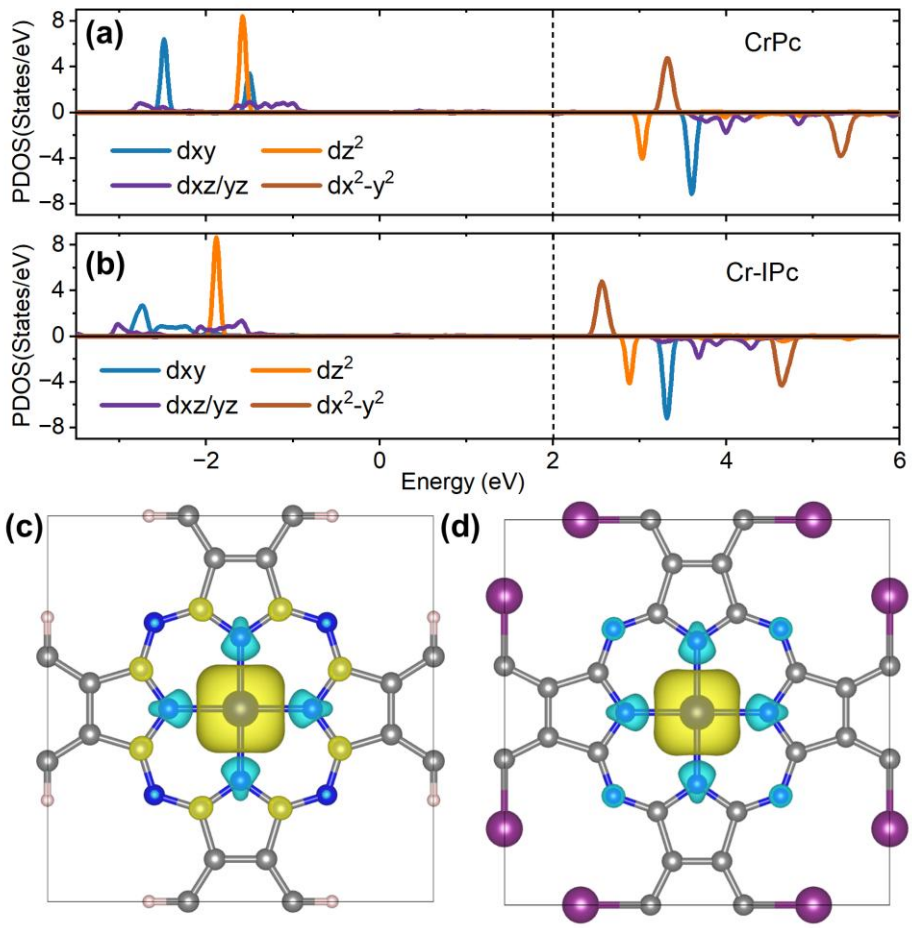

Fig. S5. Iodine-substitution-induced changes in the Cr electronic structure and spin distribution. (a, b) Projected density of states (PDOS) for the Cr 3*d* orbitals in the (a) CrPc and (b) Cr-IPc frameworks. The Fermi level is set to zero. (c, d) Spin density maps of the (c) CrPc and (d) Cr-IPc frameworks. The isosurface value is set to 0.003 e/Bohr^3.

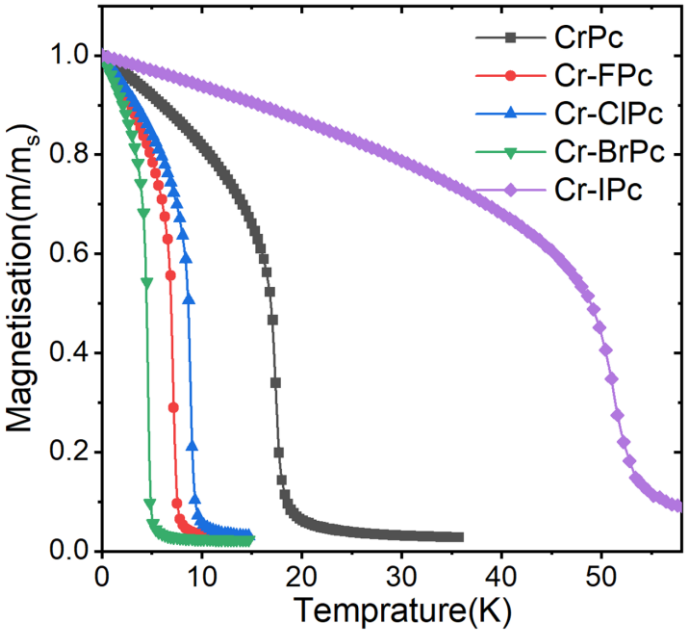

Fig. S6. Temperature dependence of the normalized magnetization for the CrPc and Cr-XPc (X = F, Cl, Br, I) frameworks.

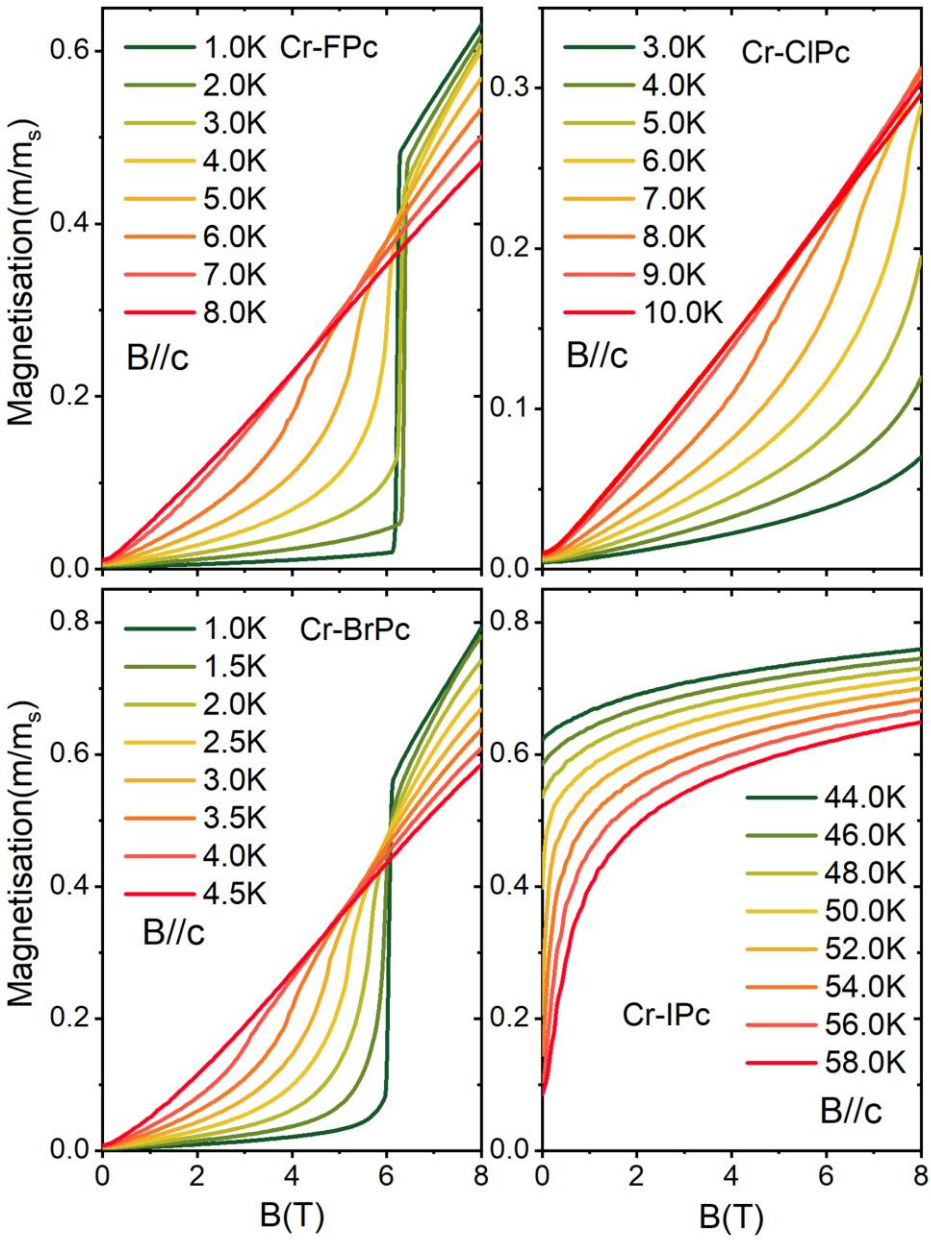

Fig. S7. Field-dependent out-of-plane magnetization of Cr-XPc frameworks. The isothermal magnetization curves are shown for Cr-XPc (X = F, Cl, Br, I) frameworks under applied magnetic fields up to 8 T along the out-of-plane direction.

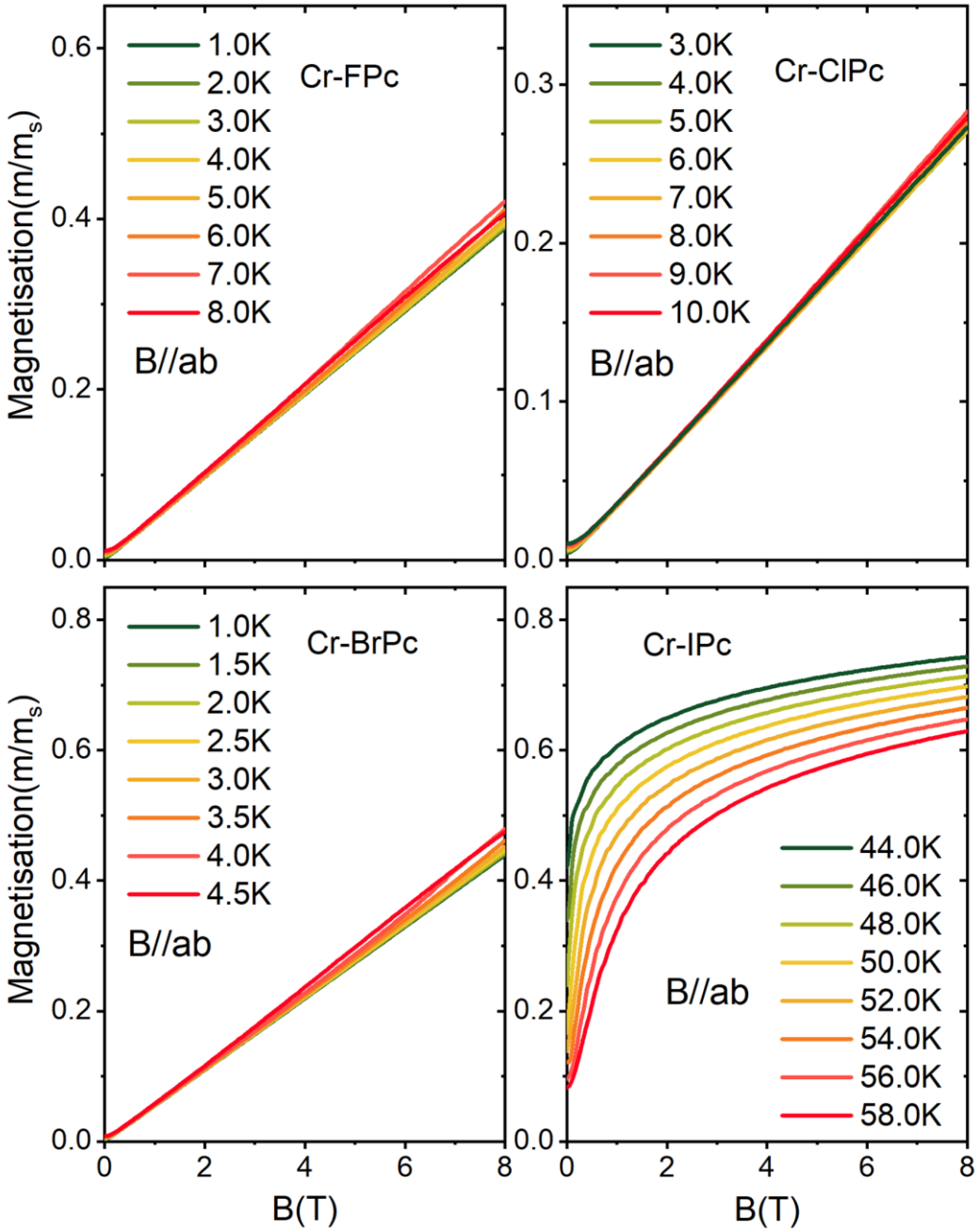

Fig. S8. Field-dependent in-plane magnetization of Cr-XPc frameworks. The isothermal magnetization curves are shown for Cr-XPc (X = F, Cl, Br, I) frameworks under applied magnetic fields up to 8 T along the in-plane direction.

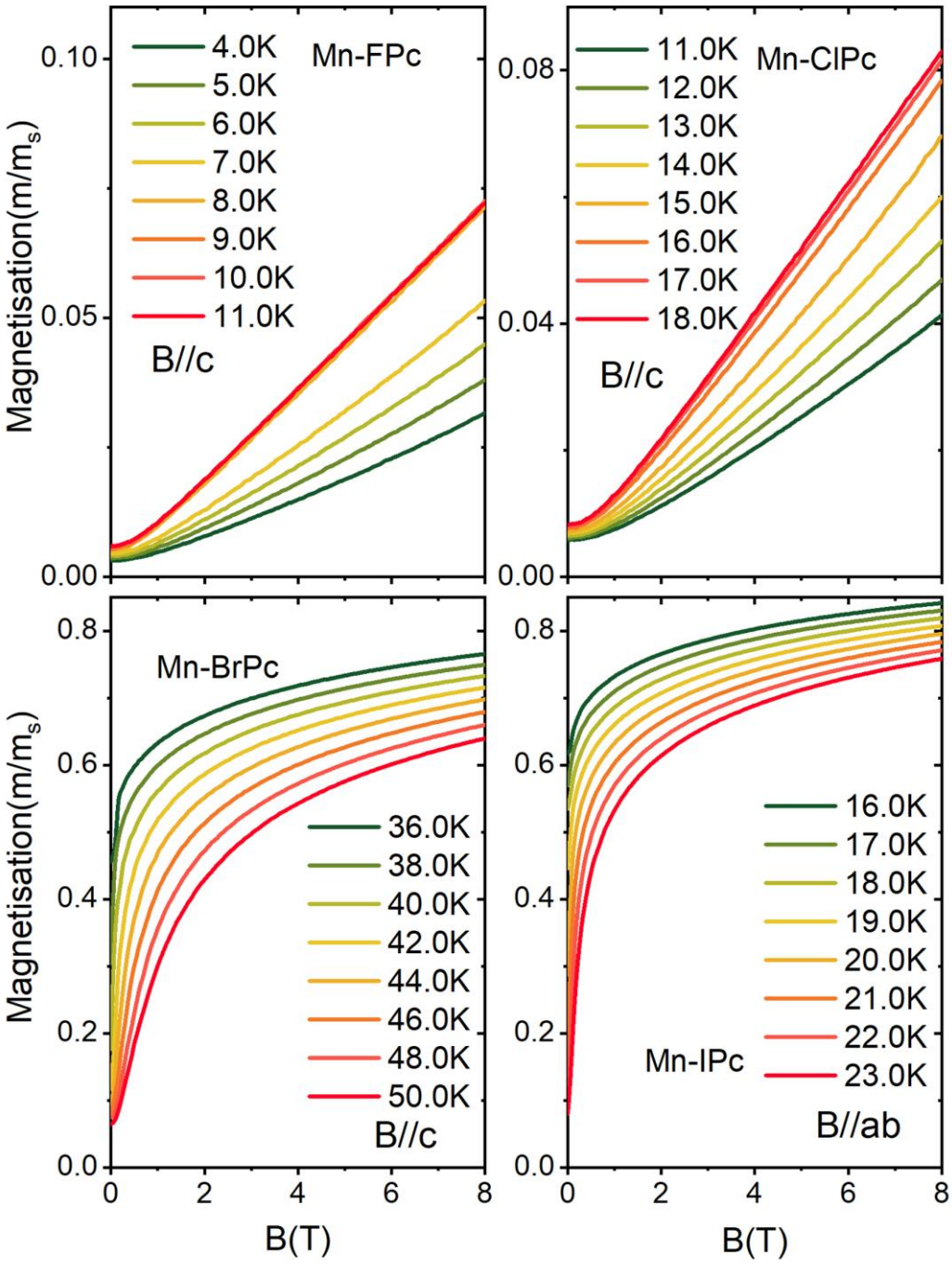

Fig. S9. Field-dependent magnetization of Mn-XPc frameworks along their easy magnetization directions. The isothermal magnetization curves are shown for Mn-XPc (X = F, Cl, Br, I) frameworks under applied magnetic fields up to 8 T.

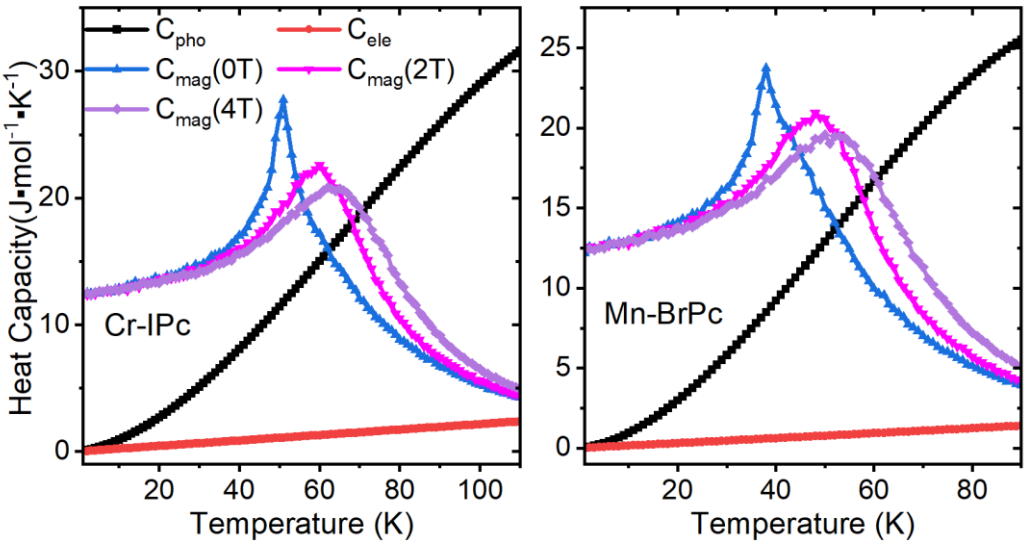

Fig. S10. Phonon, electronic, and magnetic contributions to the low-temperature heat capacity of representative M-XPc frameworks. The left panel compares the heat-capacity contributions for Cr-IPc, and the right panel compares those for Mn-BrPc. The magnetic heat capacity under external magnetic fields of 2 T and 4 T is also shown.

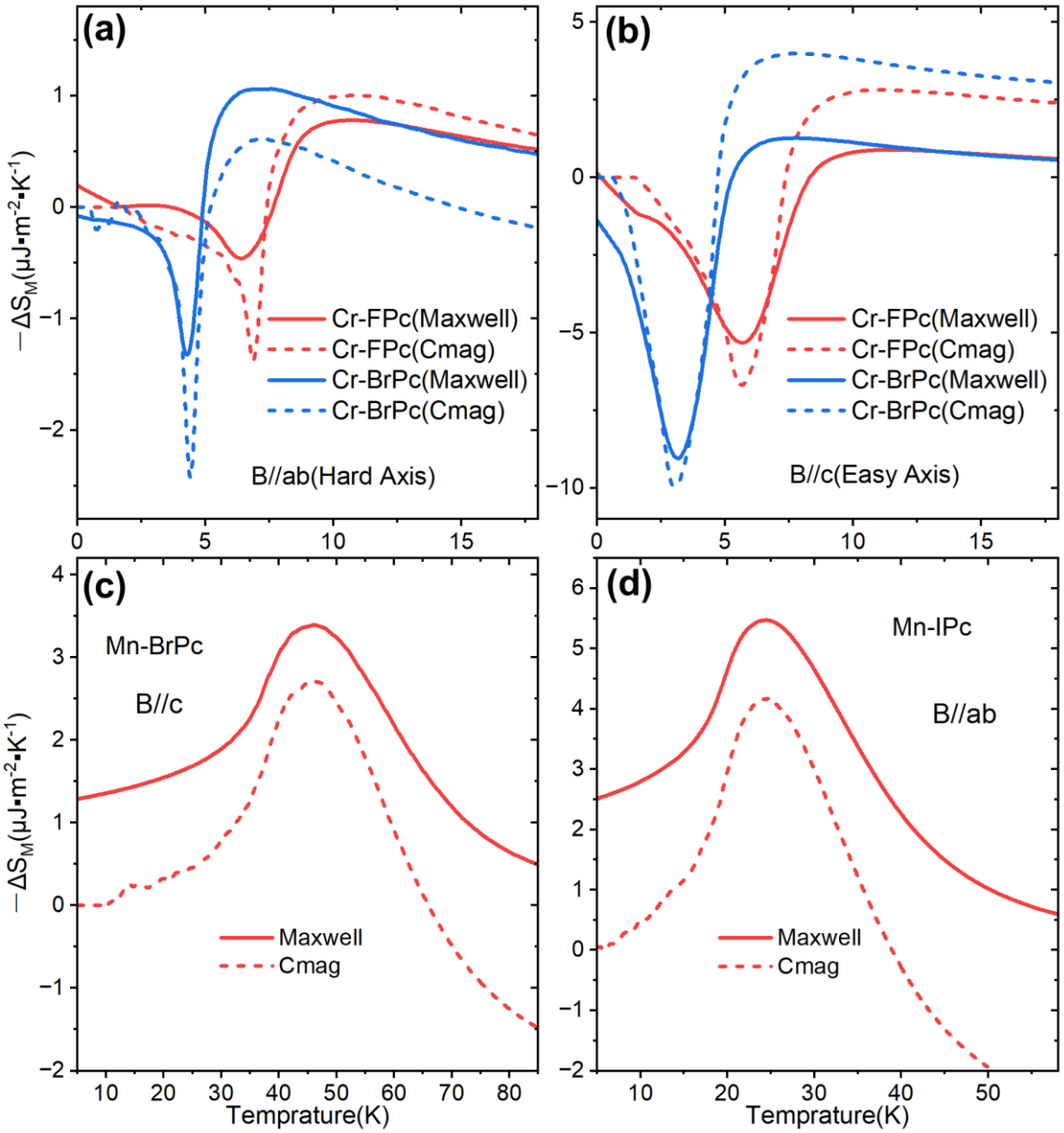

Fig. S11. Comparison of magnetic entropy changes ($-\Delta S_M$) obtained using the Maxwell-relation and heat-capacity-integration methods. The isothermal magnetic entropy change is compared under a magnetic field change of 5 T. Panels (a) and (b) show antiferromagnetic Cr-FPc and Cr-BrPc, respectively, which exhibit inverse and rotating magnetocaloric effects. Panels (c) and (d) show ferromagnetic Mn-BrPc and Mn-IPc, respectively, which exhibit conventional magnetocaloric effects.

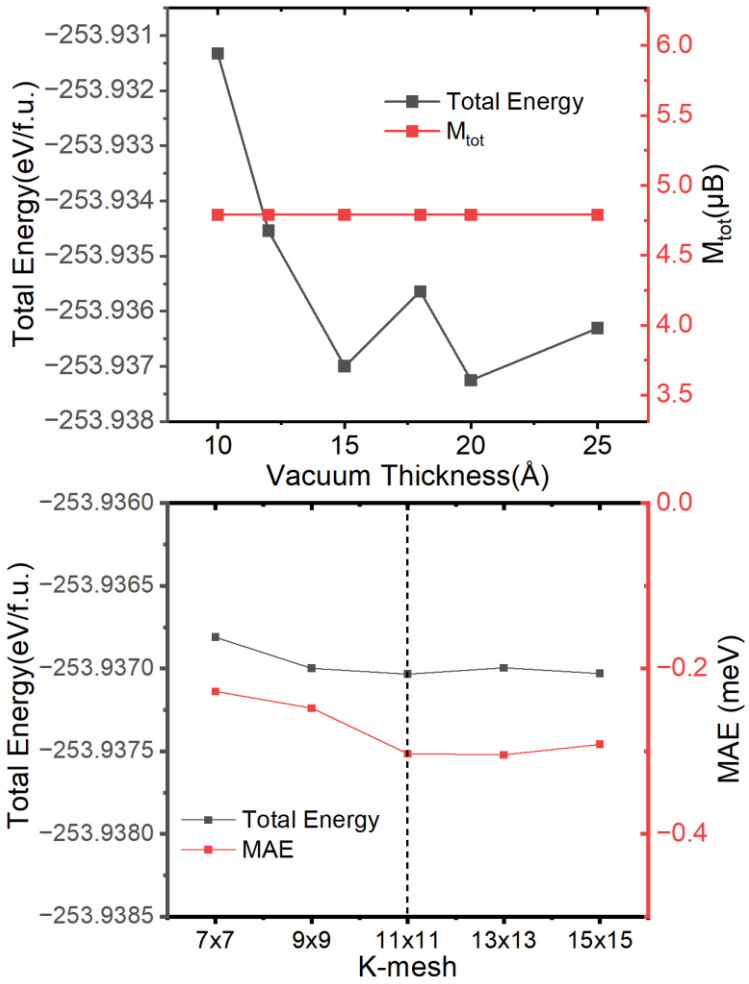

Fig. S12. Convergence tests for the DFT parameters of Mn-IPc. (Upper panel) Total energy and total magnetic moment (M_{tot}) as a function of vacuum layer thickness (10-25 Å). The total energy fluctuation falls below 1 meV/f.u. for vacuum ≥ 15 Å. (Lower panel) Total energy and magnetocrystalline anisotropy energy (MAE) as a function of k-mesh density (7×7 to 15×15). Both quantities are converged to within 0.1 meV/f.u. and 0.05 meV, respectively, for k ≥ 11×11. The adopted parameters (15 Å vacuum, 11×11 k-mesh) are indicated by dashed vertical lines.

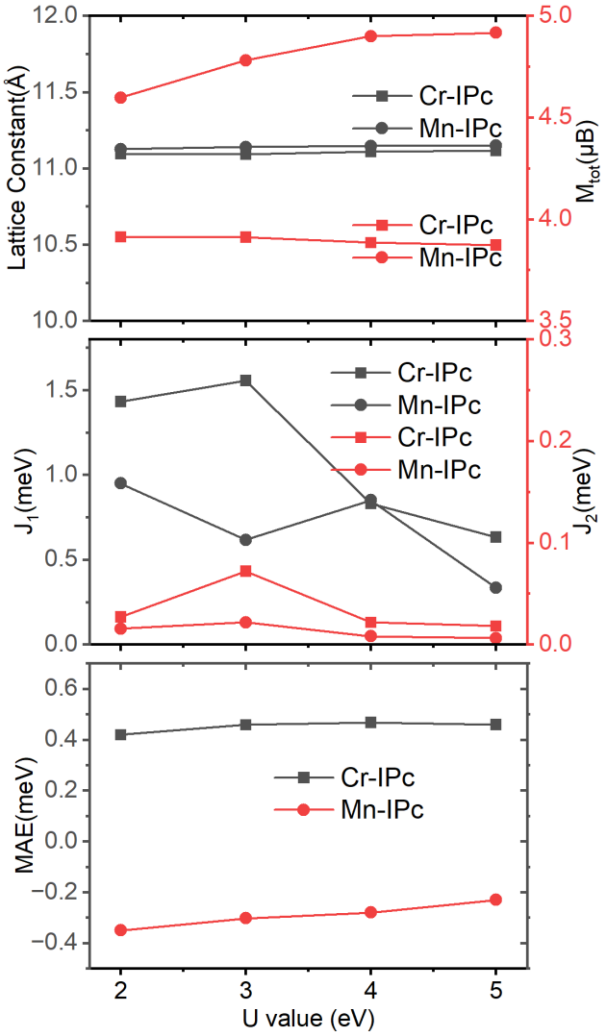

Fig. S13. Sensitivity of key physical properties of Cr-IPc and Mn-IPc to the Hubbard U parameter (U = 2, 3, 4, 5 eV). (Upper panel) Lattice constant and total magnetic moment per unit cell as a function of U value. (Middle panel) Nearest-neighbor exchange interaction parameters J_1 and J_2 as a function of U value. (Lower panel) Magnetocrystalline anisotropy energy (MAE) as a function of U value.

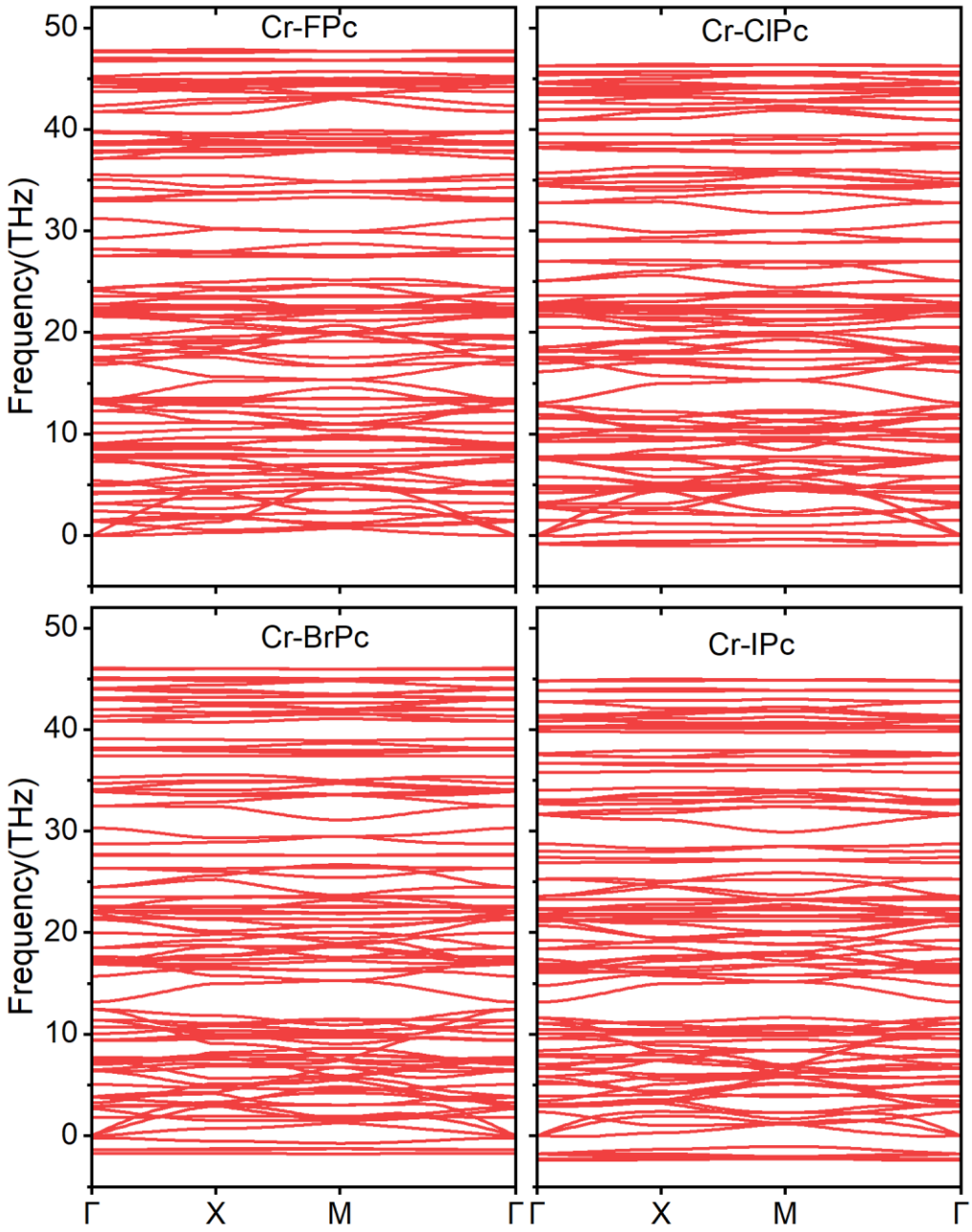

Fig. S14. Phonon spectra and dynamical stability of Cr-XPc frameworks. The phonon spectra are shown for Cr-XPc, where X denotes F, Cl, Br, or I**.**

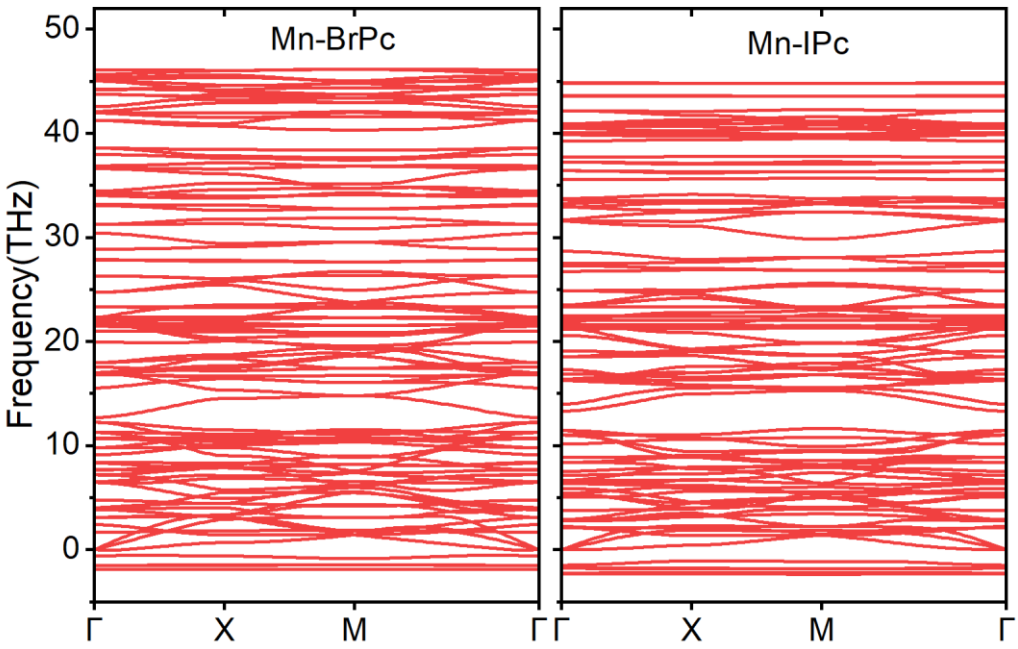

Fig. S15. Phonon spectra and dynamical stability of Mn-BrPc and Mn-IPc. The phonon spectra are shown for the Mn-BrPc and Mn-IPc frameworks.

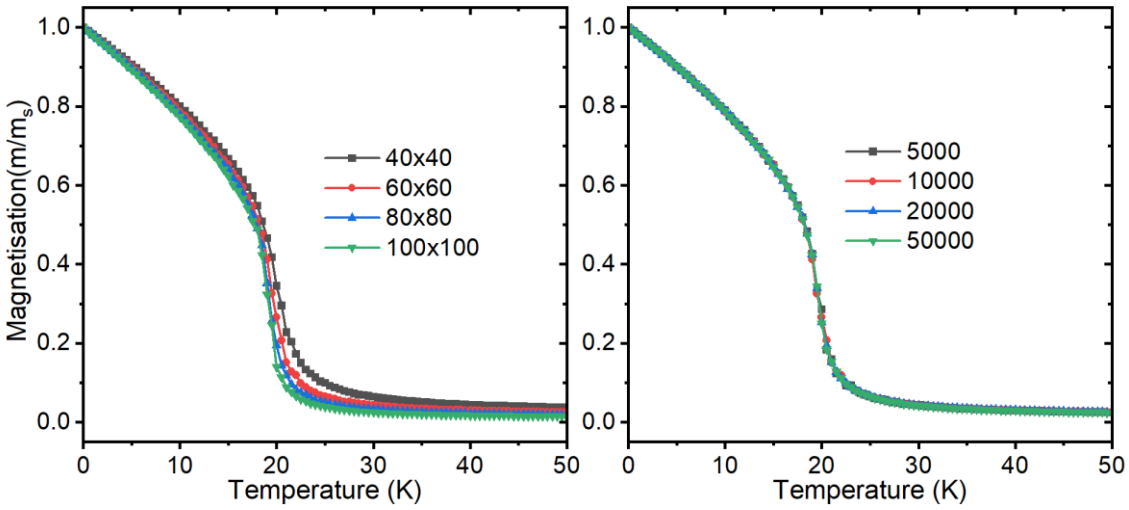

Fig. S16. Convergence tests for the Monte Carlo simulation parameters of Mn-IPc. (Left panel) Temperature dependence of the normalized magnetization for four lattice sizes (40×40, 60×60, 80×80, 100×100). The curves for 60×60 and larger are in excellent agreement, confirming convergence of the extracted T_C. (Right panel) Temperature dependence of the normalized magnetization for four MC step counts (5×10^3, 10^4, 2×10^4, and 5×10^4 steps for both thermal equilibration and statistical averaging). All curves for step count $\geq 10^4$ are essentially identical.

Table S1. Summary of the maximum magnetic entropy change ($-\Delta S_M^{\max}$, μJ·m^{-2}·K^{-1}) and peak temperature of the magnetocaloric effect (MCE) (T_{peak}, K) for the investigated MPc and M-XPc frameworks (M = Cr, Mn; X = F, Cl, Br, I). $-\Delta S_M^{\max}$ is calculated under an applied magnetic field change from 0 to 5 T along out-of-plane (B//c) and in-plane directions (B//ab), respectively. Values of $-\Delta S_M^{\max}$ are reported in both area-normalized units and mass-normalized units.

Name	B//c			B//ab		
	$-\Delta S_M^{\max}$		T_{peak}	$-\Delta S_M^{\max}$		T_{peak}
	μJ·m^{-2}·K^{-1}	J·kg^{-1}·K^{-1}	K	μJ·m^{-2}·K^{-1}	J·kg^{-1}·K^{-1}	K
CrPc	–0.59	–0.98	17.1	–0.04	–0.07	17.6
Cr-FPc	–5.32	–6.69	5.7	0.78	0.98	10.6
Cr-ClPc	–3.44	–3.53	8.1	–0.47	-0.48	8.8
Cr-BrPc	–9.04	–6.21	3.2	–1.33	–0.91	4.3
Cr-IPc	2.88	1.50	57.2	2.95	1.54	50.5
MnPc	–3.30	–5.51	18.4	–0.85	–1.42	18.9
Mn-FPc	–1.55	–1.92	7.8	–0.22	–0.27	7.8
Mn-ClPc	–0.44	–0.45	15.5	–0.05	–0.05	15.5
Mn-BrPc	3.40	2.34	45.7	3.14	2.16	45.8
Mn-IPc	5.11	2.68	19.1	5.47	2.88	24.4

Table S2. Nearest-neighbor (J_1) and next-nearest-neighbor (J_2) magnetic coupling parameters calculated with LKAG formalism. The major orbital contributions are also listed. All units are in meV.

System	J_1	Orbital Contribution		J_2	Orbital Contribution		
		$d_{yz}-d_{yz}$	$d_{xz}-d_{xz}$		$d_{yz}-d_{yz}$	$d_{xz}-d_{xz}$	$d_{xz}-d_{yz}$
CrPc	–1.22	–0.28	–0.97	0.05	0.05	0.004	0
Cr-IPc	0.88	0.72	–0.14	0.04	0.007	0.007	–0.012
MnPc	2.76	3.75	–0.96	–1.25	–0.71	–0.71	0.08
Mn-IPc	0.53	0.46	0.02	0.03	0	0	0.016

Table S3. Occupation numbers of 3*d* orbitals for the CrPc, Cr-IPc, MnPc, and Mn-IPc frameworks.

System	Spin Channel	d_{xy}	d_{yz}	d_{z^2}	d_{xz}	$d_{x^2-y^2}$
CrPc	Up	0.93	0.87	0.89	0.87	0.37
	Down	0.02	0.02	0.05	0.02	0.28
Cr-IPc	Up	0.93	0.89	0.89	0.89	0.32
	Down	0.01	0.02	0.04	0.02	0.23
MnPc	Up	0.93	0.93	0.91	0.93	0.47
	Down	0.03	0.16	0.05	0.16	0.31
Mn-IPc	Up	0.92	0.92	0.91	0.92	1.00
	Down	0.01	0.02	0.03	0.02	0.16

Table S4. Benchmark comparison of magnetocaloric parameters for representative 2D magnetic materials and their bulk van der Waals (vdW) counterparts. The table includes the maximum magnetic entropy change ($-\Delta S_M^{\max}$), peak temperature (T_{peak}), relative cooling power (RCP), and maximal adiabatic temperature change ($\Delta T_{ad}^{\max}$) for monolayer systems (from theoretical calculations) and bulk vdW materials (from experimental measurements). Monolayer values are reported in both area-normalized units and mass-normalized units. Bulk experimental values are reported only in mass-normalized units. N/A indicates data not reported in the original literature. The summarized parameters correspond to a magnetic field change of 0–5 T (refer to the original references for specific field ranges where applicable).

System	Form	$-\Delta S_M^{\max}$		T_{peak}	RCP		$\Delta T_{ad}^{\max}$	Data Source
		μJ·m^{-2}·K^{-1}	J·kg^{-1}·K^{-1}	K	μJ·m^{-2}	J·kg^{-1}	K	
CrF_3	Monolayer	35.04	22.32	21	N/A	N/A	10.98	Theory, [He 2023][1]
$CrCl_3$	Bulk, vdW	N/A	14.6	19	N/A	340.3	N/A	Exp, [Liu 2020][2]
$CrCl_3$	Monolayer	22.55	13.59	26	N/A	N/A	4.64	Theory, [He 2023][1]
$CrBr_3$	Bulk, vdW	N/A	7.2	33	N/A	191.5	2.37	Exp, [Yu 2019][3]
$CrBr_3$	Monolayer	16.07	5.94	42	N/A	N/A	1.94	Theory, [He 2023][1]
CrI_3	Bulk, vdW	N/A	4.24	61	N/A	122.6	N/A	Exp, [Liu 2018][4]
CrI_3	Monolayer	12.98	3.83	62	N/A	N/A	1.63	Theory, [He 2023][1]
$FeCl_2$	Monolayer	6.1	2.83	350	945.5	439.23	1.76	Theory, [Xie 2024][5]
$FeBr_2$	Monolayer	5.87	1.81	260	939.2	289.48	1.42	Theory, [Xie 2024][5]
$RuCl_2$	Monolayer	7.82	2.89	265	804.68	297.24	1.89	Theory, [Xie 2024][5]
$RuBr_2$	Monolayer	9.05	2.49	105	1142.21	314.30	1.10	Theory, [Xie 2024][5]
$OsCl_2$	Monolayer	8.52	2.04	535	783.84	187.42	3.86	Theory, [Xie 2024][5]
$OsBr_2$	Monolayer	10.06	2.01	360	734.38	146.57	3.44	Theory, [Xie 2024][5]
$Co_4(OH)_6(SO_4)_2[enH_2]$	Bulk	N/A	15.3	17	N/A	N/A	5.88	Exp, [Levinsky 2024][6]
Cr-FPc	Monolayer	–5.32	–6.69	5.7	18.62	23.42	-0.83	Theory, this work
Cr-BrPc	Monolayer	–9.04	–6.21	3.2	24.41	16.77	-0.82	Theory, this work
Mn-IPc	Monolayer	5.47	2.88	24.4	156.72	82.51	4.65	Theory, this work

References

[1] W. He, Y. Yin, Q. Gong, R. F. L. Evans, O. Gutfleisch, B. X. Xu, M. Yi, W. Guo, *Small* **2023**, 19, 2300333.

[2] Y. Liu, C. Petrovic, *Phys. Rev. B* **2020**, 102.

[3] X. Yu, X. Zhang, Q. Shi, S. Tian, H. Lei, K. Xu, H. Hosono, *Front. Phys.* **2019**, 14, 43501.

[4] Y. Liu, C. Petrovic, *Phys. Rev. B* **2018**, 97, 174418.

[5] W. Xie, X. Xu, F. Li, G. Zhai, Y. Yue, M. Li, H. Wang, *Appl. Phys. Lett.* **2024**, 125, 033903.

[6] J. J. B. Levinsky, B. Beckmann, T. Gottschall, D. Koch, M. Ahmadi, O. Gutfleisch, G. R. Blake, *Nat. Commun.* **2024**, 15, 8559.